Electronic Supplementary Information for

Photoelectrochemistry hydrogen production based on a Pt nanowires-bridged CdS nanorods array of piezoelectricity-triggered Z-scheme junctions

Jun Cheng, Chenpu Chen, Mingjian Chen, Qingji Xie*

Key Laboratory of Chemical Biology & Traditional Chinese Medicine Research (Ministry of Education of China), College of Chemistry and Chemical Engineering, Hunan Normal University, Changsha 410081, China

*Corresponding author.
E-mail address: xieqj@hunnu.edu.cn (Q.J. Xie)

Experimental Section

Materials and instrumentation

Acetone, ethanol, cadmium nitrate, thiourea (CH_4N_2S), glutathione (GSH), sodium phosphate, polyvinylpyrrolidone (PVP), chloroplatinic acid, sodium sulfide, titanium tetrachloride, hydrochloric acid, sulfuric acid and sodium sulfite were purchased from Sinopharm Chemical Reagent Co., Ltd. (Shanghai, China). All reagents were of analytical grade or higher purity and not further purified before use. The indium tin oxide (ITO) slices (type P003, sheet resistance < 15 Ω cm^{-2}, and the effective area of each modified ITO electrode was limited to 1 cm^2 using an insulating tape.) were purchased from Ningbo Kaiwo Photoelectric Technology Co., Ltd. (Ningbo, China). Milli-Q ultrapure water (Millipore, ≥ 18 MΩ cm) was used throughout.

A CHI660E electrochemical workstation (CH Instruments Inc., USA) and/or a ZAHNER electrochemical workstation equipped with a CIMPS-IPCE (ZAHNER, Germany) were employed in the electrochemistry, photoelectrochemistry (PEC), and/or piezoelectricity (PE)-enhanced PEC (PPEC) experiments. A gas chromatograph (GC-7900, Japan) was employed to determine the hydrogen yield. Scanning electron microscopy (SEM) images and energy dispersive spectroscopy (EDS) results were obtained on a SEM450 field emission scanning electron microscope (FEI, Czech) with EDS function. X-ray diffraction (XRD) spectra were recorded on an Ultima IV X-ray diffractometer (Rigaku, Japan) and analyzed by JCPDS standard cards. X-ray photoelectron spectroscopy (XPS) results were recorded on an Escalab-250xi X-ray photoelectron spectrometer (Thermo Fisher Scientific, USA). The Brunauer-Emmett-Teller (BET) nitrogen adsorption isotherm results were recorded on an

automatic surface area and porosity analyzer (Mack Instruments Inc., USA). Piezoresponse force microscopy (PFM) results were performed on an atomic force microscope (AFM, Shimadzu SPM9700). Ultraviolet-visible diffuse reflectance spectroscopy (UV-vis DRS, 400 ~ 800 nm) was recorded on an U-3310 UV-vis spectrophotometer (Hitachi, Japan) with $BaSO_4$ as the reference. UV-vis photoluminescence (PL) spectroscopy (450 ~ 700 nm, excited at 420 nm) was recorded on a F-4500 fluorescence spectrophotometer (Hitachi, Japan). The finite element simulation is performed on a COMSOL Multiphysics V6.0 software (COMSOL Inc., Sweden).

Preparation of the modified electrodes

The preparation of the Pt_{NW}/CdS_{NR}/ITO photoanode follows the three steps below, as shown in Scheme 1. (1) The ITO slice was ultrasonically treated in water, acetone, ethanol and water each for 10 min to remove possible surface impurities. The cleaned ITO slice was soaked in 50 mM aqueous Na_2S for 1 min, followed by washing with ethanol and ultrapure water and air drying, and then soaked in 50 mM aqueous $CdCl_2$ for 1 min, followed by washing with ethanol and ultrapure water and air drying. The above successive ionic layer adsorption and reaction (SILAR) was repeated for 10 times to obtain a dense CdS seed (CdS_{seed}) layer modified ITO substrate (CdS_{seed}/ITO). (2) The CdS_{seed}/ITO substrate was placed in an autoclave containing 5 mM $Cd(NO_3)_2$ + 5 mM CH_4N_2S + 3 mM GSH aqueous solution, and reacted at 200 ^oC for 24 h to obtain a CdS_{NR}/ITO electrode. Here, we placed the CdS_{seed}/ITO slice at a 45^o angle against the Teflon inner wall of the autoclave, with the conductive ITO surface facing down, in order to ensure the slow growth of CdS_{NR} on the CdS_{seed}/ITO surface and avoid the gravity-induced sedimentation of CdS. (3) The CdS_{NR}/ITO

electrode was placed in 0.5 mM H_2PtCl_6 + 0.3 M PVP + 0.1 M Na_3PO_4 aqueous solution, and the simultaneous Xe-lamp irradiation and 1500 rpm solution-stirring for 3 min resulted in the photodeposition of Pt_{NW} and yielded the Pt_{NW}/CdS_{NR}/ITO electrode. Here, the photogenerated electrons at the photoactive sites on the CdS_{NR} surfaces can reduce $PtCl_6^{2-}$ into Pt nanoparticles (Pt_{NP}) deposits on these photoactive sites, and the presence of Na_3PO_4 as a chelating agent and PVP as a capping agent can somewhat reduce the photoactive sites on the CdS_{NR} surfaces and can well regulate the growth of Pt_{NP} along the direction perpendicular to the CdS_{NR} surfaces to form the Pt_{NW}, as reported previously for the growth of Au nanowires (Au_{NW}) to bridge ZnO nanorods (ZnO_{NR}) in the presence of PVP and Na_3PO_4.[1]

For comparison, the CdS_{NR}/ITO electrode was placed in 0.5 mM aqueous H_2PtCl_6 (without Na_3PO_4 and PVP), and the simultaneous Xe-lamp irradiation and 1500-rpm solution-stirring for 5 min yielded the Pt_{NP}/CdS_{NR}/ITO control electrode (without any Pt bridges between the neighboring CdS_{NR}). The Pt surface area of the Pt_{NP}/CdS_{NR}/ITO control electrode was controlled to be comparable with that of the Pt_{NW}/CdS_{NR}/ITO electrode.

A TiO_2 nanorods ($TiO_{2,NR}$) array modified ITO ($TiO_{2,NR}$/ITO) electrode was prepared by placing a bare ITO substrate in an autoclave containing 4 M HCl + 0.15 M $TiCl_4$ aqueous solution for 18 h reaction at 150 ^oC.[2]

Electrochemistry and PPEC experiments

All electrochemical experiments, such as cyclic voltammetry (CV), linear sweep voltammetry (LSV), current-time (*i*-*t*) and electrochemical impedance spectroscopy (EIS) experiments were performed on a CHI660E electrochemical workstation (CH Instruments Inc., USA). The EIS was analyzed by the Z-View software (Scribner Associates Inc., USA). A

100 mW cm^{-2} Xe lamp (from a 500 W Xe lamp, CEL-M500, Ceaulight, China) was employed in the photodeposition experiments. All PEC experiments, such as LSV under chopped-light illumination, transient photocurrent density responses at 0 V *vs.* RHE constant potential, open circuit potential (E_{OC})-time (t), incident photon-electron conversion efficiency (IPCE) and Mott-Schottky experiments were performed on a ZAHNER electrochemical workstation equipped with a CIMPS-IPCE (ZAHNER, Germany), in a stirred 0.25 M Na_2S + 0.35 M Na_2SO_3 aqueous solution, and under 100 mW cm^{-2} AM 1.5G simulated sunlight illumination. The light power density of monochromatic light was measured by a series of optical filters (5 nm bandwidth, from 400 to 800 nm) and a CEL-FZ-A optical power density meter (Ceaulight, China). The conventional three-electrode system was adopted, with the bare ITO electrode or a modified ITO photoelectrode as the working electrode (WE), a Pt mesh as the counter electrode (CE), and an Ag/AgCl/KCl(sat.) electrode as the reference electrode (RE). The potentials *vs.* Ag/AgCl/KCl(sat.) are revised to those *vs.* reversible hydrogen electrode (RHE) according to $E_{RHE} = E_{Ag/AgCl/KCl(sat.)} + 0.05916pH + 0.198$ (25 ^{o}C).[3]

The H_2 gas evolved from the PEC cell was analyzed by a gas chromatograph (GC-7900, Japan) equipped with a thermal conductivity detector (TCD), with argon as the carrier gas. The electrolyte and the light source were the same as those in the above PEC measurements, and the gas products were sampled every 10 min.

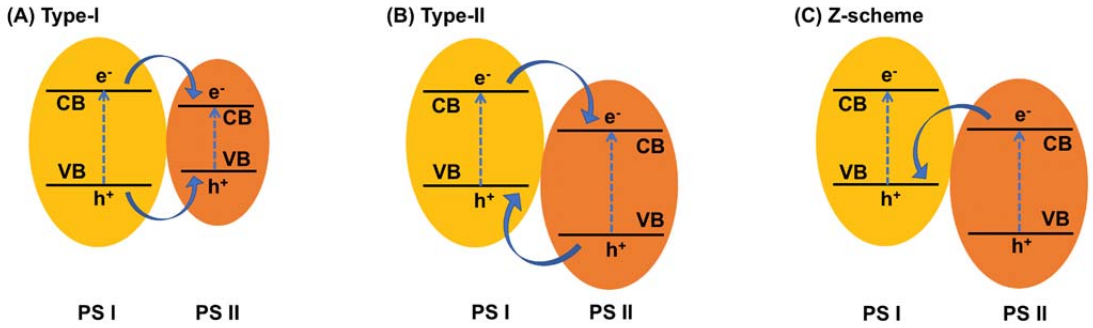

Scheme S1. Illustration of the three kinds of conventional photoelectronic heterojunctions, type-I (panel A), type-II (panel B), and Z-scheme (panel C), between two semiconductors photosystem (PS) I and PS II.[4] Here, mathematically judged from permutation and combination, the electron transfer pathways between the two semiconductors PS I and PS II can be divided only into two possible cases: (i) the CB-to-CB case (between the CB of PS I and the CB of PS II, namely, type-I and type-II), and (ii) the CB-to-VB case (between the CB of PS II and the VB of PS I, or between the CB of PS I and the VB of PS II, namely, Z-scheme). The electron-transfer pathway of the Z-scheme junction is shaped as the English letter "Z", so it is called the Z-scheme. Probably from the physical sense, the electron-transfer pathway as shown in panel C is predominant in all such direct Z-scheme junctions, because it may be difficult to skip across the intermediate energy level (i.e., the CB of PS II, which is lower than the CB of PS I but higher than the VB of PS II) to transfer the photogenerated electrons directly from the CB of PS I to the VB of PS II, but the electron transfer from the CB of PS I to this intermediate energy level has been classified to the type-II mechanism as shown in panel B.

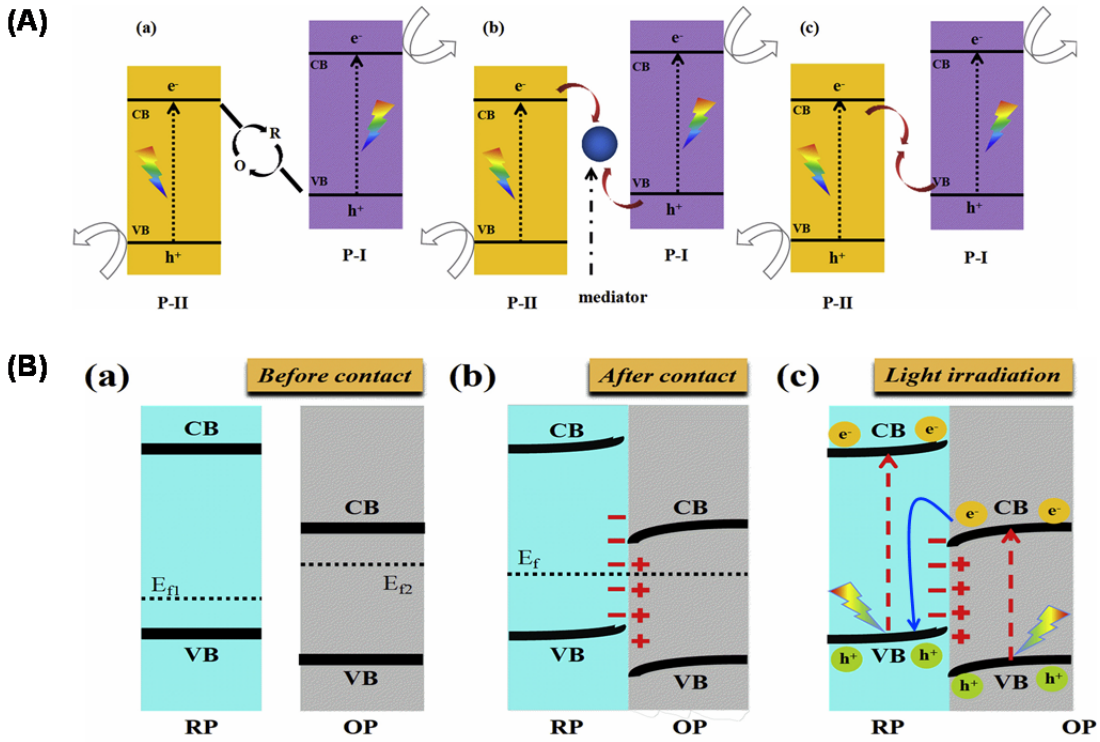

Scheme S2. Illustration of the possible charges-transfer pathways of liquid-phase Z-scheme, all-solid-state Z-scheme, and direct Z-scheme heterojunctions (A), as well as an S-scheme heterojunction (B).[5] The images here are copied from the literature.[5]

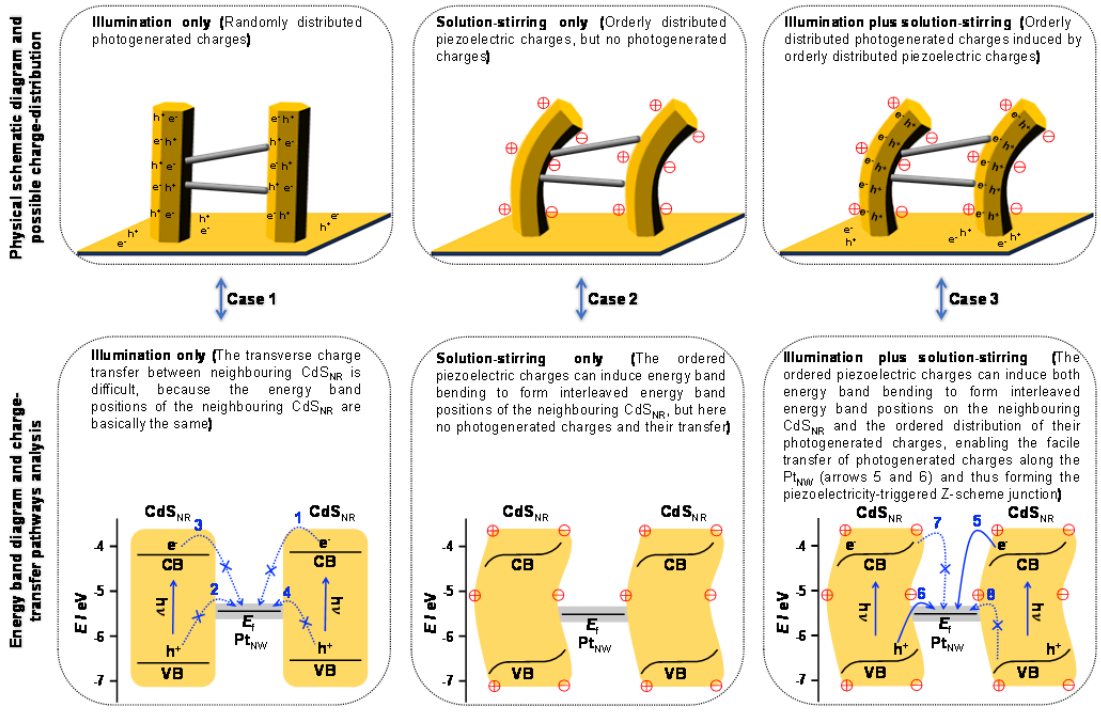

Scheme S3. Detailed illustration of the possible charge-distribution and charge-transfer pathways on the Pt_{NW}/CdS_{NR}/ITO photoanode under illumination-only (case 1), solution-stirring only (case 2), or illumination plus solution-stirring (case 3) condition. The dashed arrow with a symbol (×) denotes the unfavorable charge-transfer pathway after considering all the possible factors.

Case 1 (Illumination only): the photogenerated charges are randomly distributed on the CdS_{NR} surfaces, and the energy band positions of the neighbouring CdS_{NR} at the two ends of Pt_{NW} are basically the same. Therefore, the photogenerated electrons on the CB (photogenerated holes on the VB) of the neighbouring CdS_{NR} at both ends of the Pt_{NW} repel each other, so that the photogenerated charges cannot be effectively transferred laterally along the Pt_{NW} between the neighbouring CdS_{NR}, as reported for the ZnO_{NR}-Au_{NW}-ZnO_{NR} photoanode.[1]

Case 2 (Solution-stirring only): the piezoelectric negative charges are distributed orderly in the compression region of CdS_{NR} and the piezoelectric positive charges are distributed orderly in the tensile region of CdS_{NR}. The piezoelectric negative charges can bend the energy band upwards and the piezoelectric positive charges can bend the energy band downwards, as reported for the $MoSe_2/CdS_{NR}$ photoanode.[6] Therefore, the energy band positions distribution of CdS_{NR}-Pt_{NW}-CdS_{NR} after PE trigging is similar to that of the all-solid-state Z scheme junction $CdS/Au/TiO_2$.[7] The energy band bending by the enrichment of negative or positive charges is explained as follows, as supported by the energy band bending directions shown in Scheme S2[5] and in all the PPEC literatures we know. The compression region on the right side of the left CdS_{NR} can generate piezoelectric negative charges and thus make the energy band bend upwards, while the tensile region on the left side of the right CdS_{NR} can generate piezoelectric positive charges and thus make the energy band bend downwards, simply because a negative-charges-enriched site with a more negative potential owns a higher electron energy there and a positive-charges-enriched site with a more positive potential owns a lower electron energy there.[8] The downward bending of the energy band driven by enriched positive charges and the upward bending of the energy band driven by enriched negative charges can also be found in many relevant textbooks.

Case 3 (Illumination plus solution-stirring): the ordered distribution of piezoelectric charges causes an orderly distribution of photogenerated charges on both sides of the CdS_{NR}, and results in the interleaved energy band positions of the neighbouring CdS_{NR} at both ends of Pt_{NW}. Therefore, the enriched photogenerated CB electrons on the left side of the right CdS_{NR} can be preferentially transferred to the metal conductor Pt_{NW} (arrow 5), and the

photogenerated VB holes on the right side of the left CdS_{NR} can be preferentially transferred to the Pt_{NW} (dashed arrow 6), and then photogenerated electrons-holes recombination occurs on Pt_{NW}, leading to the easy formation of a PE-triggered Z-scheme (or S-scheme) charge-transfer pathway and thus the largest PE-enhancement factor (f_{PE} = 2.45) reported so far. Certainly, the work function values of CdS and Pt have also been considered in proposing the new concept of the PE-triggered Z-scheme (or S-scheme) CdS_{NR}-Pt_{NW}-CdS_{NR} junctions.

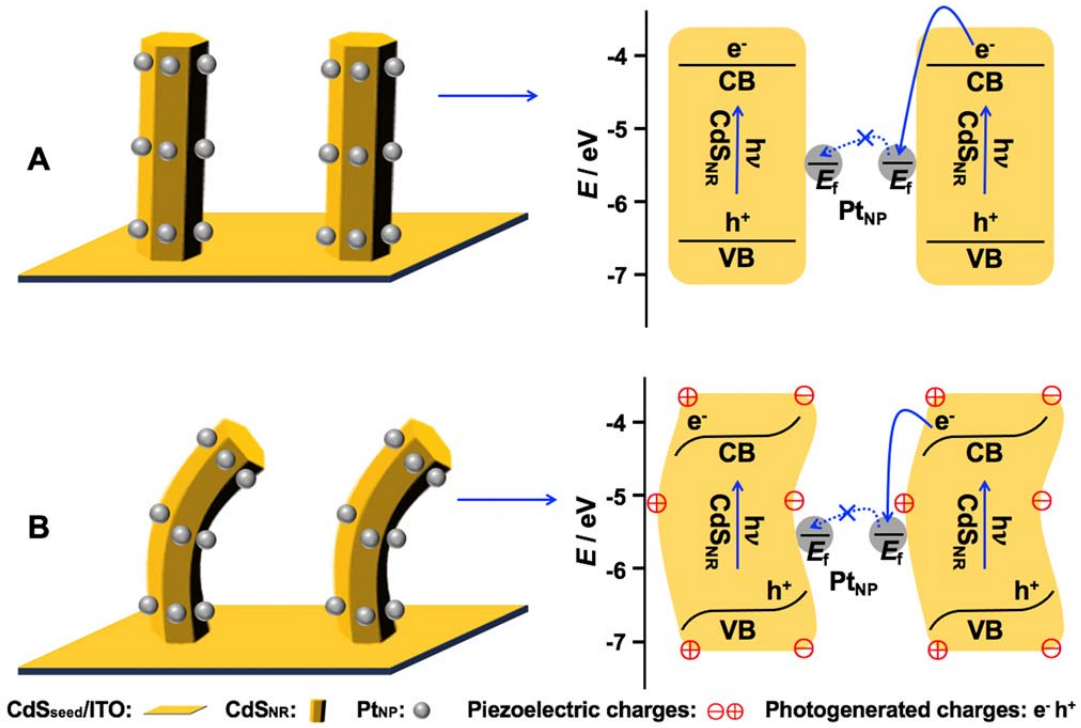

Scheme S4. Illustration of the energy band structures and the possible electron-transfer pathways on the Pt_{NP}/CdS_{NR}/ITO photoanode in an unstirred (A) or 1500-rpm-stirred (B) 0.25 M Na_2S + 0.35 M Na_2SO_3 aqueous solution under 100 mW cm^{-2} AM 1.5G simulated sunlight illumination. Here, the electrons can be photogenerated on the CB of CdS_{NR} and then be transferred to the Pt cathode due to the bias induced electric field that is vertical to the ITO surface. The photogenerated electrons on the CB of CdS_{NR} can also be transferred to the Pt_{NP} (solid arrows). Although the solution-stirring can bend the CdS_{NR} to generate piezoelectric charges and make the energy band positions of the two neighboring CdS_{NR} interleaved,[9] the transverse electron transfer between the neighboring CdS_{NR} (dashed arrows) is impossible due to the absence of the transverse electron-conductor bridges and the sufficiently large CdS_{NR}-to-CdS_{NR} spatial distance against the photogenerated electrons' tunneling.

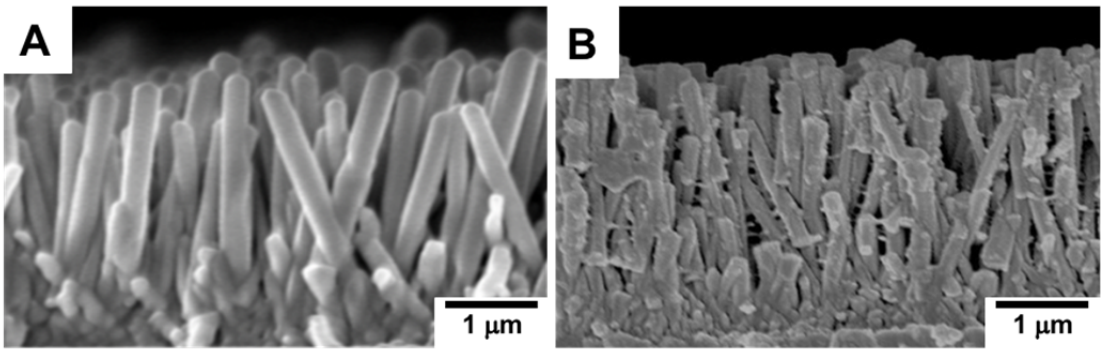

Fig. S1. The cross-section SEM images of the CdS_{NR}/ITO and Pt_{NW}/CdS_{NR}/ITO electrodes. Here, the CdS_{NR}/ITO and Pt_{NW}/CdS_{NR}/ITO electrodes show that the CdS_{NR} grow vertically on the ITO surface, and the Pt_{NW} grow on the sides of the CdS_{NR} and can bridge two neighbouring CdS_{NR}.

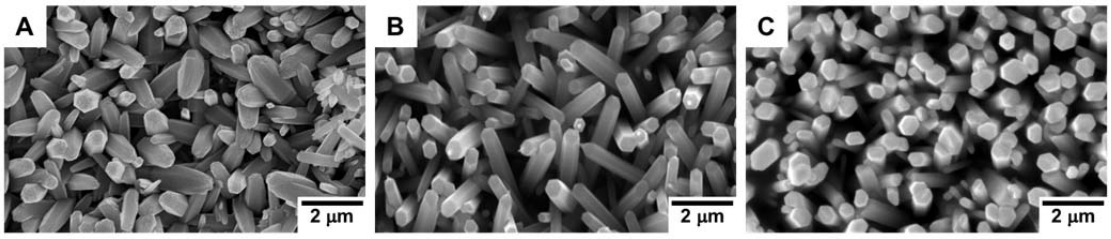

Fig. S2. SEM images of the CdS_{NR}/ITO electrode without a CdS seed layer (A), with a CdS seed layer after 5 SILAR cycles (B) and with a CdS seed layer after 10 SILAR cycles (C).

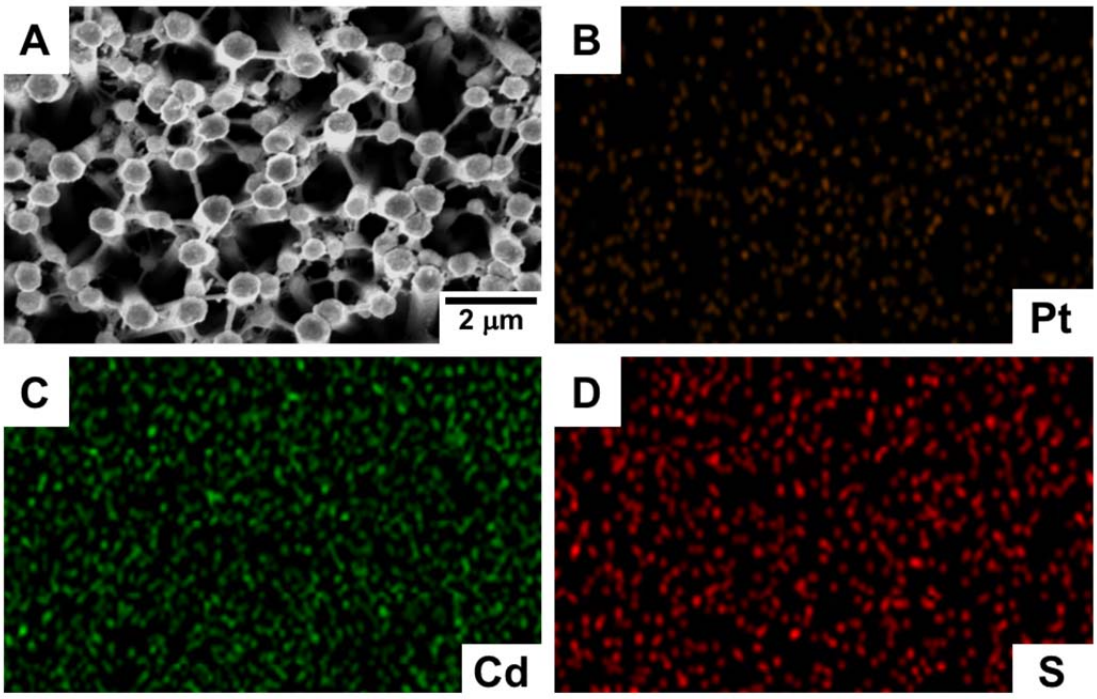

Fig. S3. SEM and corresponding EDS mapping (Cd, S, and Pt) images of the as-prepared Pt_{NW}/CdS_{NR}/ITO electrode.

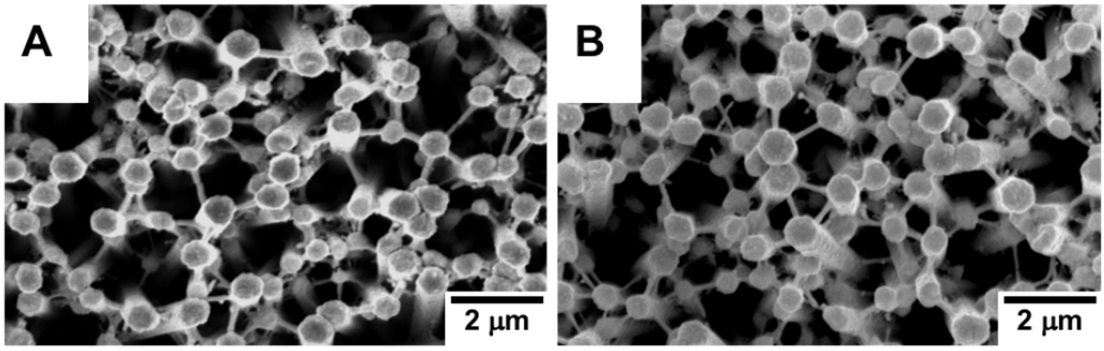

Fig. S4. SEM images of the as-prepared Pt_{NW}/CdS_{NR}/ITO photoanode (A) and this photoanode after PPEC hydrogen production for 24 h (B).

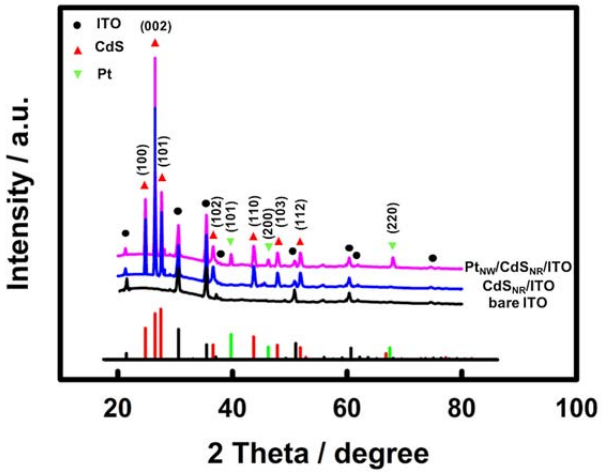

Fig. S5. XRD spectra of the bare ITO, CdS_{NR}/ITO and Pt_{NW}/CdS_{NR}/ITO electrodes. Here, the XRD peaks of the bare ITO are in good agreement with those of standard ITO (JCPDS No. 71-2195). In addition to the XRD peaks of the ITO, the seven new peaks at 24.8°, 26.5°, 27.5°, 36.6°, 43.7°, 47.8° and 51.8° on the CdS_{NR}/ITO electrode can be assigned to the (100), (002), (101), (102), (110), (103) and (112) crystal planes of CdS, respectively, according to the standard card of hexagonal wurtzite structure CdS (JCPDS No. 41-1049). These sharp XRD peaks indicate the good crystallinity. Besides the XRD peaks of the ITO and CdS, the three new peaks at 39.7°, 46.2° and 67.45° on the Pt_{NW}/CdS_{NR}/ITO electrode can be assigned to the (101), (200) and (220) crystal planes of the Pt, according to the standard card of Pt (JCPDS No. 04-0802).

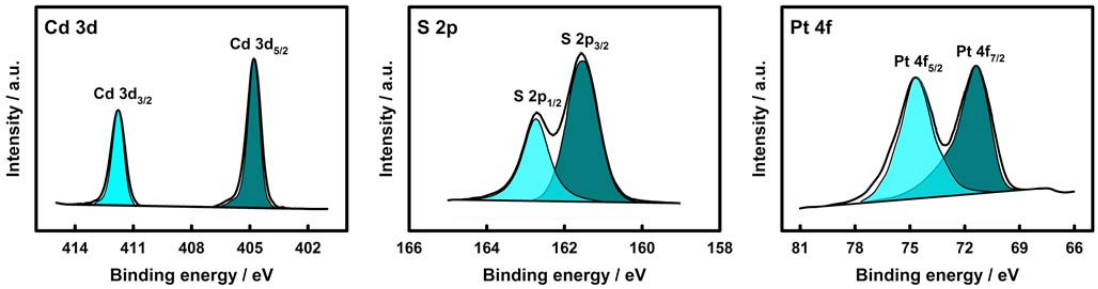

Fig. S6. XPS spectra of Cd 3d, S 2p and Pt 4f of the Pt_{NW}/CdS_{NR}/ITO electrode. Here, the two peaks at 411.8 eV and 404.6 eV are attributed to Cd $3d_{5/2}$ and Cd $3d_{3/2}$ of Cd^{2+}, respectively.[10] The two peaks at 162.7 eV and 161.5 eV are attributed to S $2p_{3/2}$ and S $2p_{1/2}$ of S^{2-}, respectively.[11] The two peaks at 74.8 eV and 71.2 eV are attributed to Pt $4f_{7/2}$ and Pt $4f_{5/2}$ of Pt^0, respectively.[12]

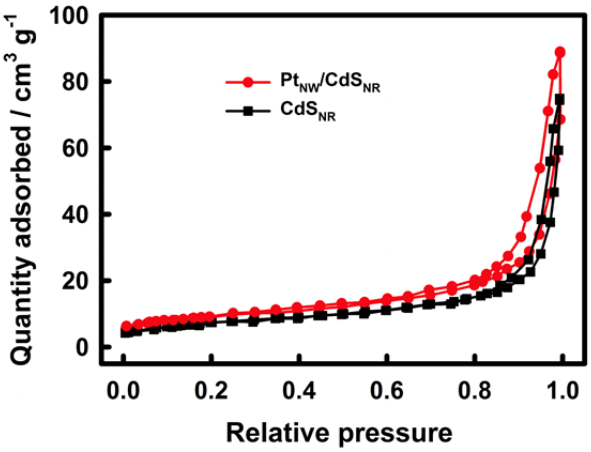

Fig. S7. BET curves of the CdS_{NR} and Pt_{NW}/CdS_{NR} samples, which were scraped off from the surfaces of CdS_{NR}/ITO and Pt_{NW}/CdS_{NR}/ITO electrodes. Here, the CdS_{NR}/ITO and Pt_{NW}/CdS_{NR}/ITO electrodes have strong adsorption capacity in the relative-pressure range from 0.9 to 1.0. It clearly shows that all tested samples can be categorized as type IV isotherms with H3 hysteresis loops.[13] In addition, the adsorption of nitrogen increased rapidly when the relative pressure is close to 1.0, indicating a large number of mesopores in the sample. At the same time, there is a chiseled H3 hysteresis ring according to the IUPAC classification, which further explains the existence of mesoporous structure. The specific surface areas of CdS_{NR} and Pt_{NW}/CdS_{NR} samples were 32 m^2 g^{-1} and 41 m^2 g^{-1}, respectively, indicating that, as expected, the photodeposition of Pt_{NW} on the CdS_{NR} can roughen the surface.

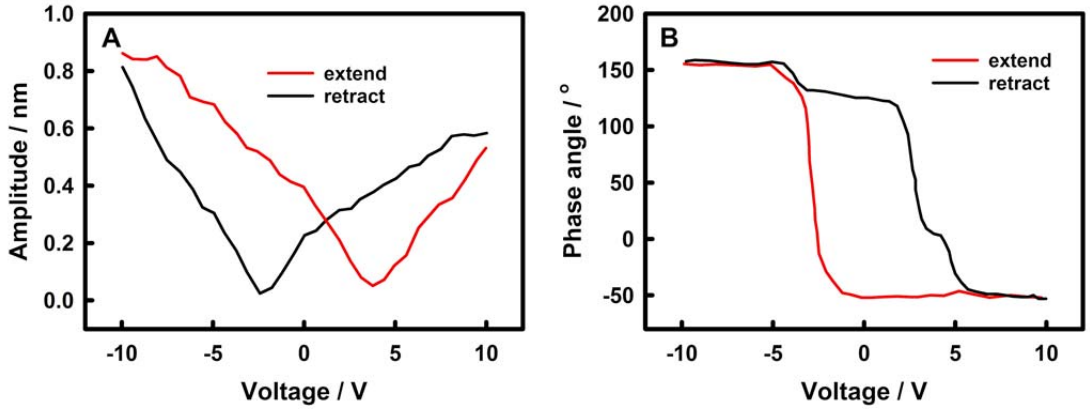

Fig. S8. PFM amplitude (A) and phase angle (B) versus voltage curves of the CdS_{NR}/ITO electrode. Here, the amplitude curves of the CdS_{NR}/ITO electrode under alternating voltage excitation show a typical butterfly-shape, and the phase angle curves show a hysteresis loop, indicating that the CdS_{NR}/ITO electrode has good piezoelectric activity.[14]

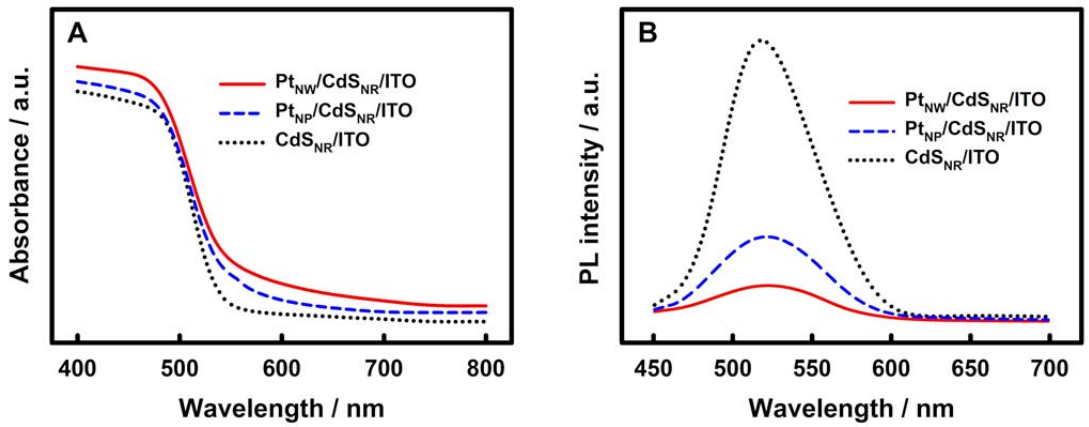

Fig. S9. (A) UV-vis DRS and (B) PL spectra excited at 420 nm for the CdS_{NR}/ITO, Pt_{NP}/CdS_{NR}/ITO and Pt_{NW}/CdS_{NR}/ITO electrodes. Here, the CdS_{NR}/ITO electrode can absorb visible light below *ca.* 530 nm, because CdS is a narrow band gap semiconductor (*ca.* 2.4 eV)[15]. The Pt_{NP}/CdS_{NR}/ITO and Pt_{NW}/CdS_{NR}/ITO electrodes have the wider light absorption range and the greater absorption intensity, due to the absorption/scattering of visible light by the Pt_{NW} and the Pt_{NP}.[1] The CdS_{NR}/ITO electrode shows an emission peak at *ca.* 525 nm, due to the de-excitation of photoexcited electrons from the CB level to the VB level.[16] The visible light emission peaks of the Pt_{NP}/CdS_{NR}/ITO and Pt_{NW}/CdS_{NR}/ITO electrodes become weaker, because the Schottky junctions can be formed between CdS_{NR} and Pt_{NW} (or Pt_{NP}) to promote the separation and transfer of photogenerated charges of CdS and can thus better suppress the de-excitation of photoexcited electrons from the CB level to the VB level, being similar to the case of loading Pt onto CdS powders.[17]

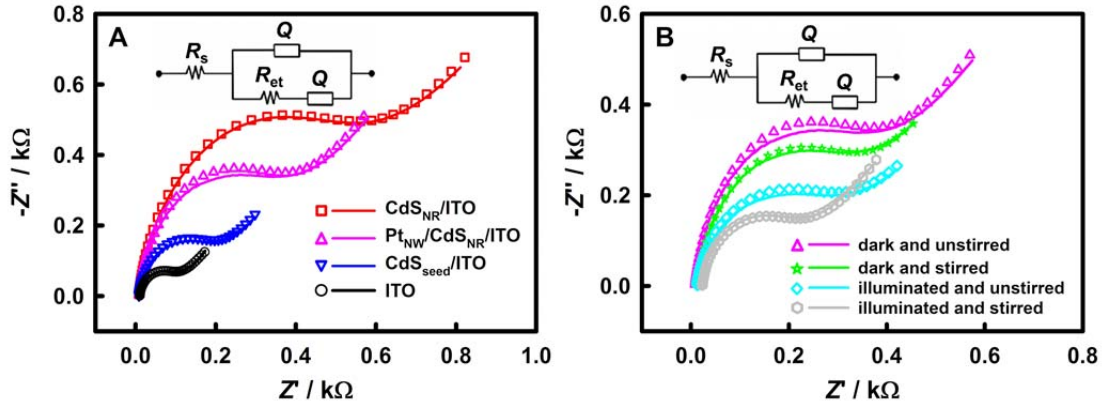

Fig. S10. (A) EIS results of the bare ITO, CdS_{seed}/ITO, CdS_{NR}/ITO and Pt_{NW}/CdS_{NR}/ITO electrodes in 0.5 M aqueous Na_2SO_4 containing 2.0 mM $K_4[Fe(CN)_6]$ under dark and unstirred conditions; (B) EIS results of the Pt_{NW}/CdS_{NR}/ITO electrode in 0.5 M aqueous Na_2SO_4 containing 2.0 mM $K_4[Fe(CN)_6]$. Initial potential = 0.24 V *vs.* Ag/AgCl/KCl(sat.) (formal potential), quiet time = 200 s (to ensure a 1:1 $[Fe(CN)_6]^{3-/4-}$-concentration ratio near the electrode surface during EIS measurements), and amplitude = 10 mV. Symbols: experimental; curves: fitted to the modified Randles equivalent circuit (Inset). Here, the R_{et} values follow the order CdS_{NR}/ITO (863 Ω) > Pt_{NW}/CdS_{NR}/ITO (572 Ω) > CdS_{seed}/ITO (268 Ω) > ITO (124 Ω), because the modification of the semiconductor materials CdS_{seed} and CdS_{NR} on the ITO electrode will reduce the electron-conductance of the electrode surface and increase the R_{et}, while the modification of the Pt_{NW} on the CdS_{NR}/ITO electrode will increase the electron-conductance of the electrode surface and reduce the R_{et}. In addition, the effects of illumination and/or solution-stirring on the R_{et} of Pt_{NW}/CdS_{NR}/ITO electrode were investigated, as shown in Fig. S10B. The R_{et} values follow the order Pt_{NW}/CdS_{NR}/ITO (dark and unstirred, 572 Ω) > Pt_{NW}/CdS_{NR}/ITO (dark and stirred, 468 Ω) > Pt_{NW}/CdS_{NR}/ITO (illuminated and unstirred, 362 Ω) > Pt_{NW}/CdS_{NR}/ITO (illuminated and stirred, 281 Ω), because solution-stirring can bend the PE-active CdS_{NR} to generate the piezoelectric field, and light

illumination can lead to the separation and transfer of the photogenerated charges of the CdS_{NR}.[12]

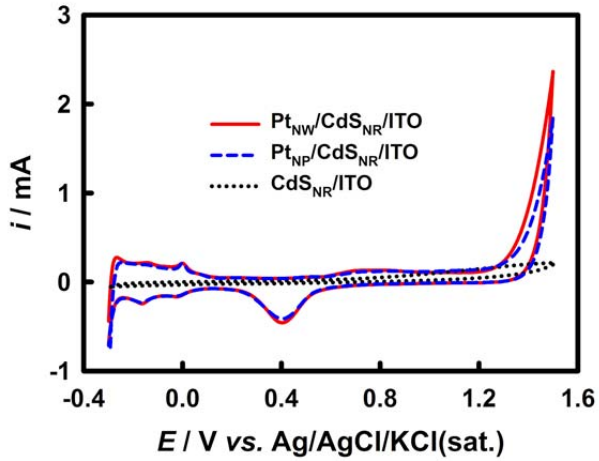

Fig. S11. CV curves on the CdS_{NR}/ITO, Pt_{NP}/CdS_{NR}/ITO and Pt_{NW}/CdS_{NR}/ITO electrodes in 0.1 M aqueous H_2SO_4. Scan rate: 50 mV s^{-1}. Here, the CdS_{NR}/ITO gave no redox peaks, and the Pt_{NW}/CdS_{NR}/ITO electrode (prepared by 3 min photodeposition in the 1500-rpm-stirred 0.5 mM H_2PtCl_6 + 0.3 M PVP + 0.1 M Na_3PO_4 aqueous solution) and the Pt_{NP}/CdS_{NR}/ITO control electrode (prepared by 5 min photodeposition in the 1500-rpm-stirred 0.5 mM aqueous H_2PtCl_6) gave comparable hydrogen underpotential ad-/de-sorption peaks. By using the conversion factor 210 μC cm^{-2},[18] the Pt active surface area of the Pt_{NW}/CdS_{NR}/ITO and Pt_{NP}/CdS_{NR}/ITO electrodes are calculated to be 1.11 cm^2 and 1.02 cm^2, respectively. The comparable Pt active surface areas of the Pt_{NW}/CdS_{NR}/ITO electrode and the Pt_{NP}/CdS_{NR}/ITO control electrode can minimize the difference of the possible chemical catalysis effects of the Pt_{NW} and the Pt_{NP} and thus ensure the reliable discussion on the relationship between the PE-triggered CdS_{NR}-Pt_{NW}-CdS_{NR} Z-scheme junctions and the PPEC performance.

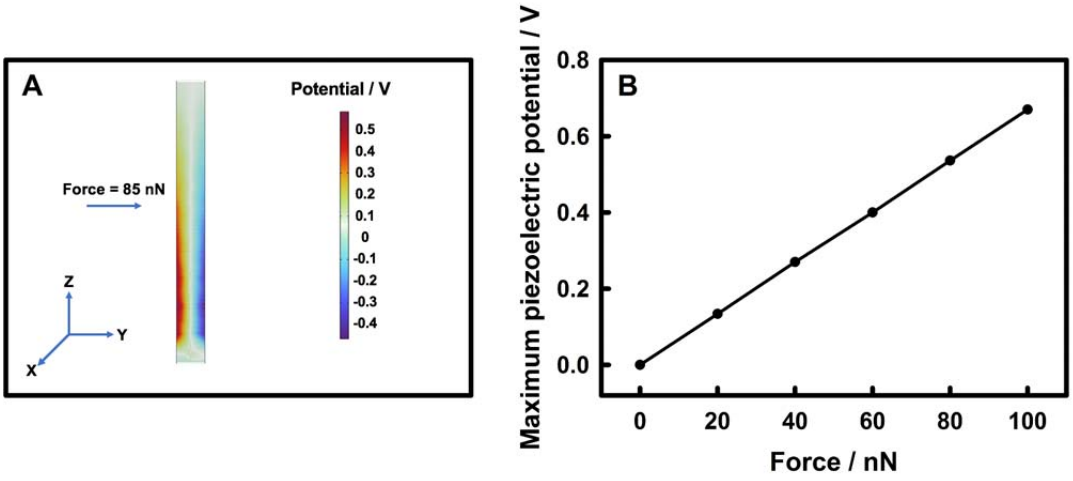

Fig. S12. (A) The finite element simulation of piezoelectric potential distribution of a CdS_{NR} sample at a force of 85 nN. (B) The force-dependent maximum piezoelectric potential responses of the CdS_{NR} sample. Here, all piezoelectric parameters of CdS_{NR} are adopted from the COMSOL Multiphysics V6.0 software for CdS. The size of CdS_{NR} is set to 200 nm × 2500 nm, the bottom of CdS_{NR} is fixed and grounded. When an external force of 85 nN is applied along the surface of the Y-axis model, the maximum piezoelectric potential of CdS_{NR} is ca. 0.57 V. The finite element simulation indicates that the increase of the applied force can increase the piezoelectric potential, implying that the increase of solution-stirring rate can increase the piezoelectric potential of the Pt_{NW}/CdS_{NR}/ITO electrode, which is more favorable for the separation and transfer of photogenerated charges to improve the PEC performance. In our opinion, unlike the photogenerated charges of redox activity, the piezoelectric charges (somewhat like the tethered "ionic charges") themselves cannot give a notable current here but can enhance the PEC process.

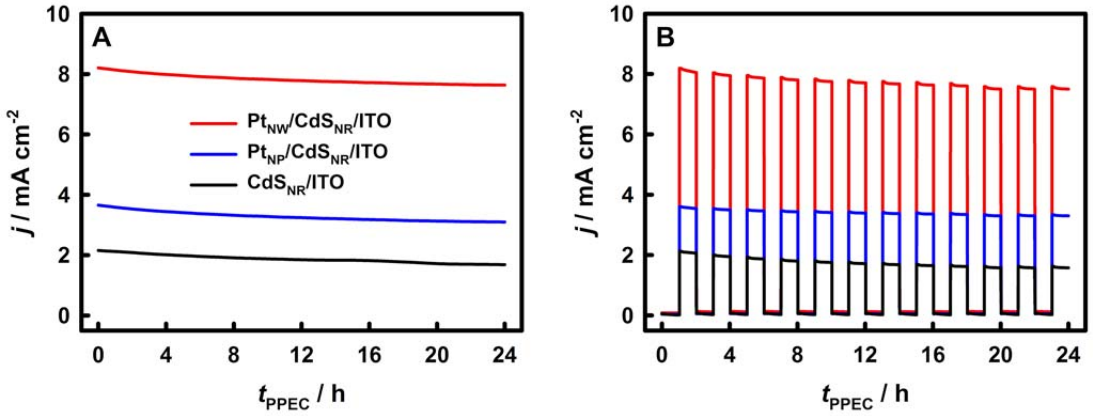

Fig. S13. (A) Current density (j)-time (t) curves under continuous light illumination and under chopped-light illumination (B, 1 h switch time) of the $Pt_{NW}/CdS_{NR}/ITO$, $Pt_{NP}/CdS_{NR}/ITO$ and CdS_{NR}/ITO electrodes at 0 V *vs.* RHE in 0.25 M Na_2S + 0.35 M Na_2SO_3 aqueous solution stirred at 1500 rpm under 100 mW cm^{-2} AM 1.5G simulated sunlight illumination.

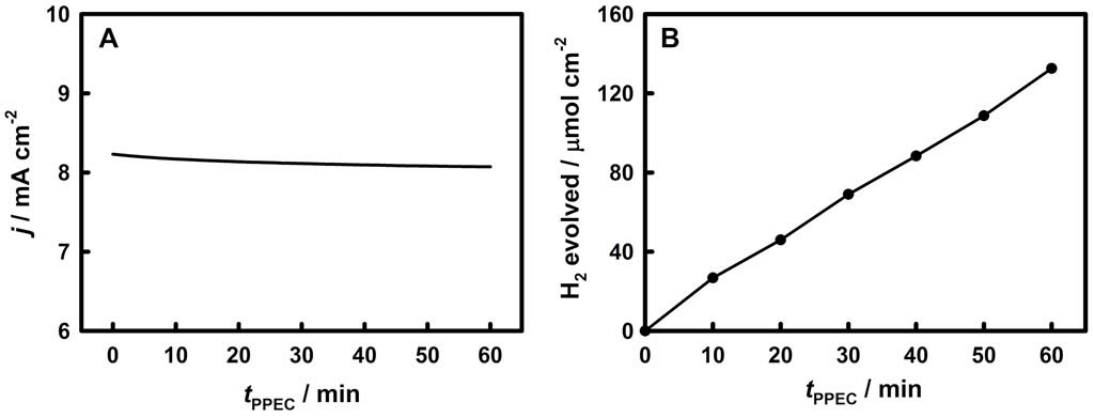

Fig. S14. Photocurrent density on the Pt_{NW}/CdS_{NR}/ITO photoanode (A) and the corresponding molar quantity of the H_2 evolved on the Pt cathode (B) at 0 V *vs.* RHE in 0.25 M Na_2S + 0.35 M Na_2SO_3 aqueous solution stirred at 1500 rpm under 100 mW cm^{-2} AM 1.5G simulated sunlight illumination. Here, the molar quantity of the evolved H_2 (n) can be calculated according to the ideal gas law (the Clapeyron equation) $n = PV/RT$ where P is the standard atmospheric pressure (101325 Pa), V is the volume of H_2 evolved (in m^3), n is the molar quantity (in mol), R is the molar gas constant (8.314 J mol^{-1} K^{-1}), and T is the thermodynamic temperature (298.15 K).

The corresponding molar quantity of H_2 (n) can be electrochemically calculated according to the reaction $2H^+ + 2e^- = H_2$. The theoretical electric charge (Q') corresponding to the generation of n mol H_2 can be calculated from the Faraday law of electrolysis, $Q' = zFn$, where z is the number of electrons transferred during PPEC hydrogen production ($z = 2$), and F is the Faraday constant (96485.3 C mol^{-1}). The Faraday efficiency (η) is thus calculated according to $\eta = Q'/Q \times 100\%$ where Q is the experimental electric charge by integrating the photocurrent versus time curve, as shown in Fig. S14A.

At 60 min in Fig. S14B, we obtain V = 3.22 mL, n = 0.132 mmol, Q' = 25.4 C, and Q = 29.0 C, so η = 87.6%.

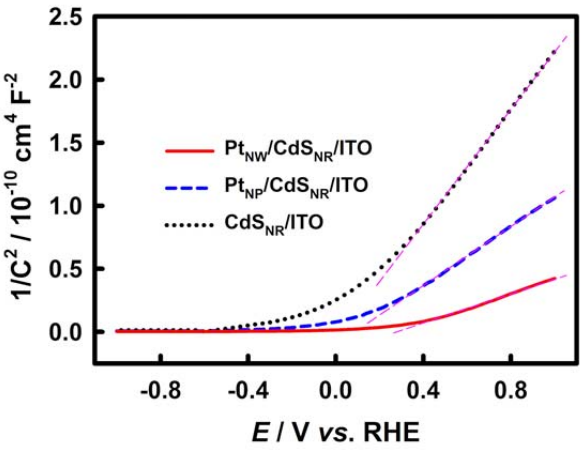

Fig. S15. Mott-Schottky curves of the Pt_{NW}/CdS_{NR}/ITO, Pt_{NP}/CdS_{NR}/ITO and CdS_{NR}/ITO electrodes in 0.25 M Na_2S + 0.35 M Na_2SO_3 aqueous solution stirred at 1500 rpm. Here, the carrier density (N, in cm^{-3}) of a semiconductor can be calculated according to Eq. S1,[19]

$$N = [2/(e\varepsilon\varepsilon_0)] \times [d(1/C^2)/dE]^{-1} \quad \text{(S1)}$$

where e is the charge of a single electron (1.602×10^{-19} C), ε is the relative permittivity (11.6 for CdS[20]), ε_0 is the permittivity of vacuum (8.854×10^{-14} F cm^{-1}), E is the potential (in V), and C is the capacitance density (in F cm^{-2}).

From the slopes of the ramps and Eq. S1, we obtain the $d(1/C^2)/dE$ (in cm^4 F^{-2} V^{-1}) and N (in cm^{-3}) values of 5.94×10^9 cm^4 F^{-2} V^{-1} and 2.12×10^{21} cm^{-3} for the Pt_{NW}/CdS_{NR}/ITO electrode, 1.25×10^{10} cm^4 F^{-2} V^{-1} and 1.01×10^{21} cm^{-3} for the Pt_{NP}/CdS_{NR}/ITO electrode, and 2.11×10^{10} cm^4 F^{-2} V^{-1} and 5.97×10^{20} cm^{-3} for the CdS_{NR}/ITO electrode. The larger N value indicates that more photogenerated carriers are available for PEC applications, thus the above results imply the best PPEC performance on the Pt_{NW}/CdS_{NR}/ITO electrode at 1500 rpm.

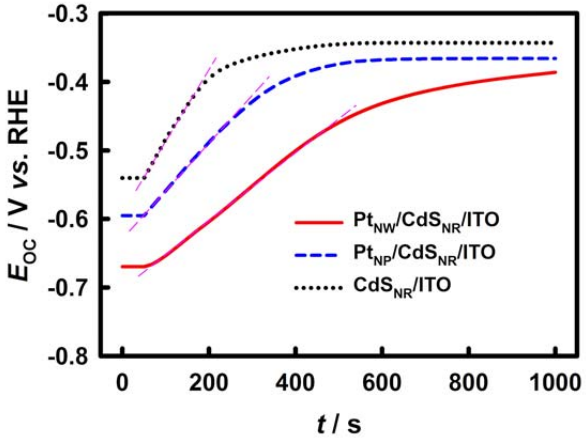

Fig. S16. Open circuit potential (E_{OC})-time (t) curves of the $Pt_{NW}/CdS_{NR}/ITO$, $Pt_{NP}/CdS_{NR}/ITO$ and CdS_{NR}/ITO electrodes in 0.25 M Na_2S + 0.35 M Na_2SO_3 aqueous solution stirred at 1500 rpm under 100 mW cm^{-2} AM 1.5G simulated sunlight illumination for 50 s. Here, the photoelectron lifetime (τ, in s) of a semiconductor can be calculated according to Eq. S2,[21]

$$\tau = (k_B T/e) \times (dE_{OC}/dt)^{-1} \quad \text{(S2)}$$

where k_B is the Boltzmann constant (1.381×10^{-23} J K^{-1}), T is the temperature (298.15 K), e is the charge of a single electron (1.602×10^{-19} C), t is the time (in s), and E_{OC} is the open circuit potential (in V).

From the slopes of the ramps and Eq. S2, we obtain the dE_{OC}/dt (in V s^{-1}) and τ (in ns) values of 4.95×10^{-4} V s^{-1} and 52 ns for the $Pt_{NW}/CdS_{NR}/ITO$ electrode, 6.97×10^{-4} V s^{-1} and 37 ns for the $Pt_{NP}/CdS_{NR}/ITO$ electrode, and 1.15×10^{-3} V s^{-1} and 22 ns for the CdS_{NR}/ITO electrode. The larger τ value indicates that the longer lifetime of photogenerated carriers, thus the above results imply the best PPEC performance on the $Pt_{NW}/CdS_{NR}/ITO$ electrode at 1500 rpm.

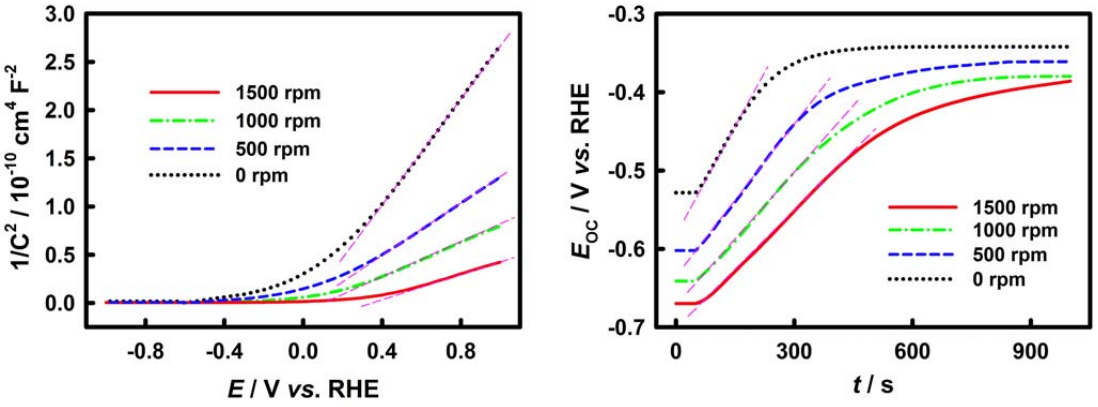

Fig. S17. Mott-Schottky and E_{OC}–t curves of the Pt_{NW}/CdS_{NR}/ITO electrode in 0.25 M Na_2S + 0.35 M Na_2SO_3 aqueous solution stirred at 0 rpm, 500 rpm, 1000 rpm or 1500 rpm under 100 mW cm^{-2} AM 1.5G simulated sunlight illumination. Here, from the slopes of the ramps and Eqs. S1 and S2, we obtain the N (in cm^{-3}) and τ (in ns) values of 2.12×10^{21} cm^{-3} and 52 ns for the Pt_{NW}/CdS_{NR}/ITO-1500 rpm, 1.68×10^{21} cm^{-3} and 44 ns for the Pt_{NW}/CdS_{NR}/ITO-1000 rpm, 9.98×10^{20} cm^{-3} and 36 ns for the Pt_{NW}/CdS_{NR}/ITO-500 rpm and 5.12×10^{20} cm^{-3} and 28 ns for the Pt_{NW}/CdS_{NR}/ITO-0 rpm. The larger N and τ values indicate that the greater density and longer lifetime of photogenerated carriers, thus the above results imply the best PPEC performance on the Pt_{NW}/CdS_{NR}/ITO electrode at 1500 rpm.

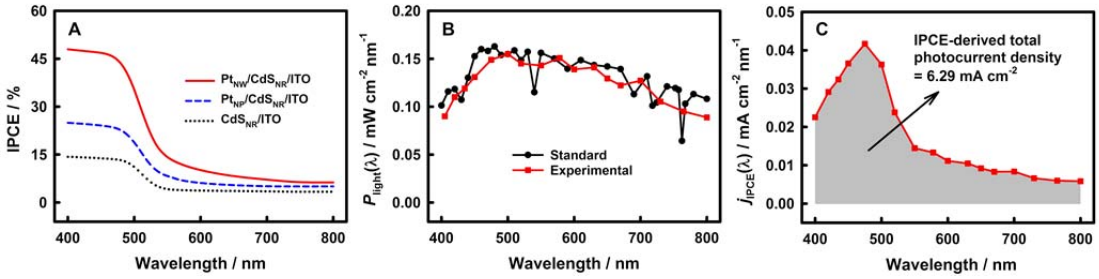

Fig. S18. (A) IPCE versus wavelength curves of the $Pt_{NW}/CdS_{NR}/ITO$, $Pt_{NP}/CdS_{NR}/ITO$ and CdS_{NR}/ITO electrodes potentiostatically at 0 V *vs*. RHE in 0.25 M Na_2S + 0.35 M Na_2SO_3 aqueous solution stirred at 1500 rpm under 100 mW cm^{-2} AM 1.5G simulated sunlight illumination. (B) Incident light power density per nm ($P_{light}(\lambda)$) versus incident light wavelength measured by using a series of optical filters (5 nm bandwidth, from 400 to 800 nm) and an optical power density meter under 100 mW cm^{-2} AM 1.5G simulated sunlight illumination, and the standard 100 mW cm^{-2} AM 1.5G simulated solar spectrum in this wavelength range is shown for comparison. (C) IPCE-derived photocurrent density per nm ($j_{IPCE}(\lambda)$, calculated from the data shown in Fig. S18A and S18B according to the IPCE equations below), versus incident light wavelength for the $Pt_{NW}/CdS_{NR}/ITO$ electrode.

Fig. S18A shows the IPCE values of the $Pt_{NW}/CdS_{NR}/ITO$ electrode at different wavelength measured by the ZAHNER electrochemical workstation. We measured the spectrum of $P_{light}(\lambda)$ versus incident light wavelength by using a series of optical filters (5 nm bandwidth, from 400 to 800 nm) and an optical power density meter under 100 mW cm^{-2} AM 1.5G simulated sunlight illumination, which agrees well with the standard 100 mW cm^{-2} AM 1.5G simulated solar spectrum in this wavelength range,[22] as shown in Fig. S18B. The $j_{IPCE}(\lambda)$ versus incident light wavelength (Fig. S18C) can be calculated from the IPCE values (Fig.

S18A) and the $P_{light}(\lambda)$ values (Fig. S18B) at different wavelength. The $j_{IPCE}(\lambda)$ of a semiconductor can be calculated according to Eq. S3,[23]

$$j_{IPCE}(\lambda) = \frac{IPCE(\lambda) \times \lambda \times P_{light}(\lambda)}{1240} \quad (S3)$$

where IPCE(λ) is the incident photon-electron conversion efficiency at the incident light wavelength λ (%), λ is the incident light wavelength (in nm), N_e is the number of electrons, N_p is the number of photons, $j_{IPCE}(\lambda)$ is the IPCE-derived photocurrent density per nm at the incident light wavelength λ (in mA cm^{-2} nm^{-1}), t is the time (in s), e is the charge of a single electron (1.602×10^{-19} C), $P_{light}(\lambda)$ is the incident light power density per nm at the incident light wavelength (in mW cm^{-2} nm^{-1}), h is the Planck constant (6.626×10^{-34} J s), v is the incident light frequency (in Hz), and c is the light speed (2.998×10^{8} m s^{-1}).

As shown in Fig. S18C, the IPCE-derived total photocurrent density calculated by integrating the $j_{IPCE}(\lambda)$ from 400 nm to 800 nm is 6.29 mA cm^{-2}, which is, as expected, somewhat smaller than but still comparable with the experimental PPEC photocurrent density of 8.13 mA cm^{-2}, because the PPEC measurement was carried out under AM 1.5G simulated sunlight illumination (ideally with the full wavelength from *ca.* 305 to *ca.* 4045 nm, actually from 300 to 1100 nm for our light source), though the PEC-active wavelength range of the Pt_{NW}/CdS_{NR}/ITO electrode matches acceptably with that shown in Fig. S18C. The IPCE-derived total photocurrent density of 6.29 mA cm^{-2} and the experimental PPEC photocurrent density of 8.13 mA cm^{-2} are thus rational, indicating the reliability of the PPEC data reported in this research.

Table S1. PPEC water splitting performance of representative PE-enhanced photoanodes*

Photoanode	Electrolyte solution	Applied potential (V *vs.* RHE)	Photocurrent density without the deformation induced PE (mA cm^{-2})	Photocurrent density with PE (mA cm^{-2})	PE-enhancement factor (f_{PE})	Reference
WO_3/ZnO_{NR}/ITO	1 M Na_2SO_4	1.23	2.39	3.38	1.41	[24]
Co-Pi/ZnO_{NR}/ITO	0.1 M Na_2SO_4	1.23	0.58	0.80	1.38	[12]
$Ag_2O/BaTiO_3/TiO_{2,NR}$/ITO	1 M NaOH	1.0	1.51	1.80	1.20	[25]
WO_3/CdS_{NR}/ITO	0.25 M Na_2S + 0.35 M Na_2SO_3	0	2.13	3.42	1.61	[26]
$CdS_{S,NR}$/ITO	0.25 M Na_2S + 0.35 M Na_2SO_3	0	2.24	3.09	1.38	[27]
Pt_{NP}/CdS_{NR}/ITO	0.25 M Na_2S + 0.35 M Na_2SO_3	0	2.56	3.64	1.42	This work
Pt_{NW}/CdS_{NR}/ITO	0.25 M Na_2S + 0.35 M Na_2SO_3	0	3.32	8.13	2.45	This work

*NR: nanorods, NS: nanosheets, NW: nanowires, Co-Pi: cobalt-phosphate, PVDF: poly(vinylidene fluoride), PMN-PT: $[(PbMg_{0.33}Nb_{0.67}O_3)_{1-x} : (PbTiO_3)_x]$, $CdS_{S,NR}$: CdS nanosheets with S-vacancy.

References (The numbering here is only valid for the Supplementary Information)

1. T. Wang, B. J. Jin, Z. B. Jiao, G. X. Lu, J. H. Ye and Y. P. Bi, *J. Mater. Chem. A*, 2014, **2**, 15553-15559.

2. B. Liu and E. S. Aydil, *J. Am. Chem. Soc.*, 2009, **131**, 3985-3990.

3. X. Zhang, Y. Liu and Z. H. Kang, *ACS Appl. Mater. Interfaces*, 2014, **6**, 4480-4489.

4. J. X. Low, J. G. Yu, M. Jaroniec, S. Wageh and A. A. Al-Ghamdi, *Adv. Mater.*, 2017, **29**, 1601694.

5. Y. Yuan, R. T. Guo, L. F. Hong, X. Y. Ji, Z. D. Lin, Z. S. Li and W. G. Pan, *Mater. Today Energy*, 2021, **21**.

6. Q. Han, Z. Han, Y. Wang, S. Zhang, J. Fang, H. Li and P. Fang, *J. Colloid Interface Sci.*, 2023, **630**, 460-472.

7. A. Iwase, Y. H. Ng, Y. Ishiguro, A. Kudo and R. Amal, *J. Am. Chem. Soc.*, 2011, **133**, 11054-11057.

8. Y. Y. Wen, J. Chen, X. Gao, H. A. Che, P. F. Wang, B. Liu and Y. H. Ao, *Nano Energy*, 2022, **101**, 107614.

9. L. Pan, S. C. Sun, Y. Chen, P. H. Wang, J. Y. Wang, X. W. Zhang, J. J. Zou and Z. L. Wang, *Adv. Energy Mater.*, 2020, **10**, 2000214.

10. L. Ma, K. Chen, F. Nan, J. H. Wang, D. J. Yang, L. Zhou and Q. Q. Wang, *Adv. Funct. Mater.*, 2016, **26**, 6076-6083.

11. Z. M. Song, X. D. Zhu, Y. S. Zeng, A. Z. Wang, S. K. Li, Y. Fan, M. D. Cai, Q. Cheng, Y. X. Wei and S. Sun, *Catal. Lett.*, 2020, **150**, 1878-1889.

12. S. C. Zhang, Z. F. Liu, M. N. Ruan, Z. G. Guo, L. E, W. Zhao, D. Zhao, X. F. Wu and D. M. Chen, *Appl. Catal. B-Environ.*, 2020, **262**, 118279.

13. C. Z. Sun, H. Zhang, H. Liu, X. X. Zheng, W. X. Zou, L. Dong and L. Qi, *Appl. Catal. B-Environ.*, 2018, **235**, 66-74.

14. X. W. Wang, X. X. He, H. F. Zhu, L. F. Sun, W. Fu, X. L. Wang, L. C. Hoong, H. Wang, Q. S. Zeng, W. Zhao, J. Wei, Z. Jin, Z. X. Shen, J. Liu, T. Zhang and Z. Liu, *Science Advances*, 2016, **2**, e1600209.

15. X. Wang, C. Liow, D. Qi, B. Zhu, W. R. Leow, H. Wang, C. Xue, X. Chen and S. Li, *Adv. Mater.*, 2014, **26**, 3506-3512.

16. K. H. Cho and Y. M. Sung, *Nano Energy*, 2017, **36**, 176-185.

17. J. H. Yang, H. J. Yan, X. L. Wang, F. Y. Wen, Z. J. Wang, D. Y. Fan, J. Y. Shi and C. Li, *J. Catal.*, 2012, **290**, 151-157.

18. S. Trasatti and O. A. Petrii, *Pure Appl. Chem.*, 1991, **63**, 711.

19. F. X. Xiao and B. Liu, *Nanoscale*, 2017, **9**, 17118-17132.

20. S. C. Zhang, Z. F. Liu, M. N. Ruan, Z. G. Guo, L. E, W. Zhao, D. Zhao, X. F. Wu and D. M. Chen, *Applied Catalysis B-Environmental*, 2020, **262**, 118279.

21. J. Bisquert, A. Zaban, M. Greenshtein and I. Mora-Sero, *J. Am. Chem. Soc.*, 2004, **126**, 13550-13559.

22. J. W. Sun, D. K. Zhong and D. R. Gamelin, *Energ. Environ. Sci.*, 2010, **3**, 1252-1261.

23. J. Cheng, C. P. Chen, M. J. Chen and Q. J. Xie, *Chem. Commun.*, 2022, **59**, 114-117.

24. Y. Chen, L. Wang, R. Gao, Y. Zhang, L. Pan, C. Huang, K. Liu, X. Chang, X. Zhang and J. Zou, *Appl. Catal. B-Environ.*, 2019, **259**, 9.

25. Z. R. Liu, L. W. Wang, X. Yu, J. Zhang, R. Q. Yang, X. D. Zhang, Y. C. Ji, M. Q. Wu, L. Deng, L. L. Li and Z. L. Wang, *Adv. Funct. Mater.*, 2019, **29**, 1807279.

26. Q. Y. Zhao, Z. F. Liu, J. W. Li, W. G. Yan, J. Ya and X. F. Wu, *Int. J. Hydrogen Energy*, 2021, **46**, 36113-36123.

27. Q. Y. Zhao, Z. F. Liu, Z. G. Guo, M. N. Ruan and W. G. Yan, *Chem. Eng. J.*, 2022, **433**, 133226.